Theory of infrared-dressed atomic photoionization by extremely ultraviolet attosecond pulse trains

Han Chieh Lee,* Shih Da Jheng, and Tsin Fu Jiang

Institute of Physics, National Chiao Tung University, Hsinchu 30010, Taiwan
*Corresponding author: hclee@mail.nctu.edu.tw

We theoretically study the infrared (IR)-dressed photoionization of atoms excited by extreme ultraviolet attosecond pulse trains above ionization threshold. The initial state of atoms is treated perturbatively by the IR field, and the continuum states are considered as Coulomb–Volkov (CV) waves. CV waves can much reduce the gauge difference calculated with Volkov waves, and, in general, the contribution of ground-state perturbation to the photoelectron spectrum is negligible. Our calculations show qualitative agreement with the experimental results [Phys. Rev. Lett. **95**, 013001 (2005)]. An evident dependence of the photoelectron spectrum on the delay phase between the IR field and the attosecond pulse train is exhibited in both helium and argon. The angular distribution of photoelectrons with various IR polarizations and the corresponding photoelectron spectra are presented. The linearly polarized IR fields are shown to have a higher controlling capability of the spectrum via IR delay phases than the circularly polarized fields. On the other hand, the circularly polarized IR fields have a fruitful angular dependence of photoelectrons with various IR delay phases.   © 2012 Optical Society of America

OCIS codes: 020.2649, 020.4180, 340.7480.

1. INTRODUCTION

The advent of attosecond light pulse technology opened the study of electronic dynamics in atoms with unprecedented time resolution [1,2]. Attosecond light pulses are produced with extremely ultraviolet (XUV) light, and can be sorted into attosecond pulse trains (APTs) and single attosecond pulses (SAPs). The APT consists of a series of evenly spaced infrared (IR) harmonics, as shown in Fig. 1, and is a powerful tool when combined with another IR field [3–12]. One example is the technique called Reconstruction of Attosecond Beating by Interference of Two-photon Transition (RABITT) [3], which is used to characterize the APT. By varying the delay phase between the APT and IR fields, amplitudes and phases of the APT's harmonics can be extracted from photoelectron spectra, and the APT's temporal shape is reconstructed.

The APT + IR technique also provides an opportunity for the quantum control of atomic photoionization. Johnsson *et al.* [5] showed experimentally that the IR field is efficient in controlling the photoelectron spectra excited by the APT above the atomic ionization threshold. The photoelectron born at the zero of the IR field (inset of Fig. 2) clearly shows a more extended energy distribution than that born at the peak of the IR field. Their numerical solutions of the time-dependent Schrödinger equation (TDSE) also evinced that. Otherwise, the analytic approach is generally based on the strong-field approximation, where the IR-dressed continuum state is regarded as the Volkov wave [7]. In this paper, we propose another analytic treatment for the two-color (XUV + IR) ionization based on the perturbation theory. While the IR field in the experiment [5] is not weak ($\sim 10^{13}$ W/cm²), it is still not intense enough to make the ionization as compared with that excited by the APT. Thus, we treat the IR field as a perturbation to the ground state

and consider the continuum states as Coulomb–Volkov (CV) waves. The perturbation method has been widely used for dressed issues in the past [13–17].

We show that the CV wave can much reduce the gauge difference calculated with the Volkov wave. The validity of the CV wave is examined and the effect of the ground-state perturbation is discussed. Our calculations agree with the experimental result [5] qualitatively. A significant spectral dependence on the delay phase between the IR field and the APT is shown. The model is then applied to study the IR polarization effect. We calculate the angular distribution of photoelectrons with various IR polarizations, as well as the corresponding spectra. Linearly polarized IR fields are shown to have a higher capability to control the photoelectron spectra than circularly polarized fields, while circularly polarized IR fields have a more fruitful angular dependence than linearly polarized fields. The analytical model is helpful for quantum control of photoionization [5] and the RABITT technique [3] due to the short computing time as compared with the TDSE calculations. The remainder of this paper is organized as follows. In Section 2 we present the theory for the IR-dressed XUV transition. In Section 3 we show and discuss the calculated results. Finally, conclusions are drawn in Section 4.

2. THEORY

Consider the *S*-matrix element for the XUV transition between IR-dressed atomic states:

$$S = -i \int_{-\infty}^{\infty} dt \langle \Psi_{\mathbf{k}}(\mathbf{r}, t) | H_{\text{int}}(t) | \Psi_g(\mathbf{r}, t) \rangle, \tag{1}$$

where $H_{\text{int}}(t)$ is either $\mathbf{r} \cdot \mathbf{E}_{\text{APT}}(t)$ or $\mathbf{A}_{\text{APT}}(t) \cdot \mathbf{p}/c$ for the length or velocity gauges, respectively. Unless otherwise specified, atomic units (a.u.), i.e., $e = m_e = \hbar = 1$, are used in this paper. $\mathbf{E}_{\text{APT}}(t)$ and $\mathbf{A}_{\text{APT}}(t)$ are the electric field and the vector

potential of the APT field, respectively, and c is the speed of light. The APT electric field is described by

$$\mathbf{E}_{\text{APT}}(t) = \hat{z} \sum_{\xi=-10}^{10} (-1)^{\xi} E_x \sin[\omega_x(t - \xi T_h)]$$
$$\times \exp\left[-2 \ln 2\left(\frac{t - \xi T_h}{\tau_x}\right)^2\right] \exp\left[-2 \ln 2\left(\frac{t}{\tau_T}\right)^2\right], \quad (2)$$

where $T_h = \pi/\omega_{\text{IR}}$, with $\omega_{\text{IR}} = 1.55$ eV being the IR frequency. Figure 1(a) shows an example with $\omega_x = 23$ eV and $\tau_x = 0.3$ fs, while Fig. 1(b) shows the corresponding Fourier spectra with the horizontal axis in units of ω_{IR}. Twice IR photon spacing can be found.

The IR field with a generalized polarization can be written as

$$\mathbf{E}_{\text{IR}}(t) = E_{\text{IR}}\left[\hat{z}\cos\left(\frac{\Delta}{2}\right)\sin(\omega_{\text{IR}}t + \phi_d)\right.$$
$$\left. + \hat{y}\sin\left(\frac{\Delta}{2}\right)\cos(\omega_{\text{IR}}t + \phi_d)\right], \quad (3)$$

where Δ is set to 0, π, and $\pi/2$ for the $\hat{z}$-axis, $\hat{y}$-axis, and circular polarizations in our calculations, respectively. ϕ_d is the delay phase between the IR and APT fields.
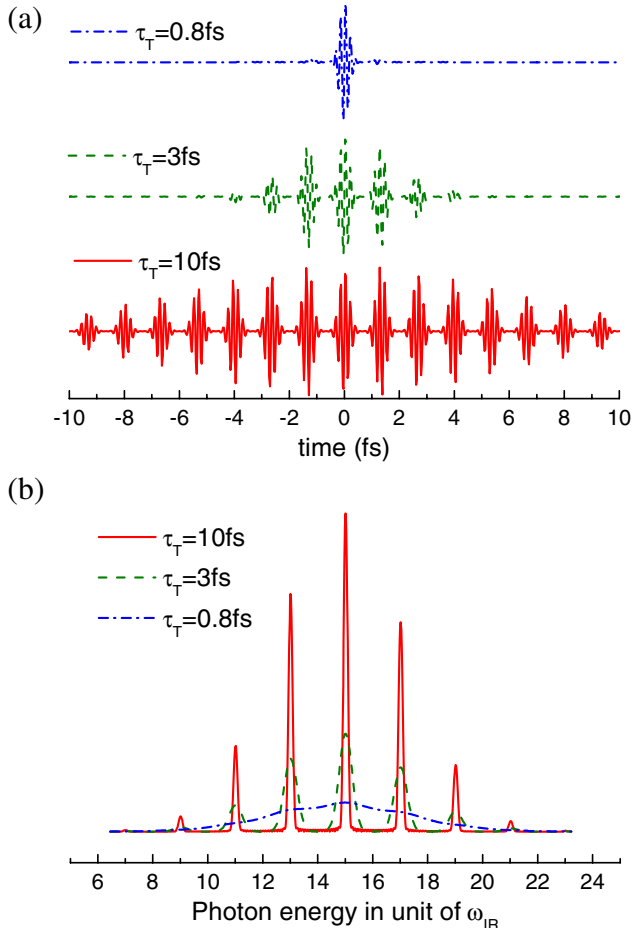

Fig. 1. (Color online) (a) Profile and (b) frequency spectrum of APT at $\omega_x = 23$ eV (central frequency), $\tau_x = 0.3$ fs (FWHM of each burst), and $T_h = \pi/\omega_{\text{IR}}$. A variation from SAP to APT by tuning τ_T (FWHM of APT) is demonstrated. FWHM: full width at half-maximum.

The IR-dressed ground state (1s for He and 3p for Ar in single-active-electron notation) can be described by the first-order perturbation as long as the IR intensity remains moderate:

$$\Psi_g^{L,V}(\mathbf{r}, t) = e^{-i\omega_g t}\left\{|\psi_g^{(0)}>\right.$$
$$+ \frac{iE_{\text{IR}}}{2}[-G(\omega_g - \omega_{\text{IR}})\hat{M}_{L,V}|\psi_g^{(0)}> e^{i(\omega_{\text{IR}}t + \phi_d)}$$
$$\left. \pm G(\omega_g + \omega_{\text{IR}})\hat{M}_{L,V}|\psi_g^{(0)}> e^{-i(\omega_{\text{IR}}t + \phi_d)}]\right\}, \quad (4)$$

where $\hat{M}_{L,V}$ is $\hat{z}\cdot\mathbf{r}$ or $\omega_{\text{IR}}^{-1}\hat{z}\cdot\nabla_{\mathbf{r}}$ for the length or velocity gauges, respectively. $|\psi_g^{(0)}\rangle$ is the unperturbed ground-state wave function and

$$G(\Omega) = \frac{1}{\Omega - \hat{H}_0} = \sum_n \frac{|\psi_n^{(0)}\rangle\langle\psi_n^{(0)}|}{\Omega - E_n}.$$

$\hat{H}_0 = \mathbf{p}^2/2 + V_M(r)$ with $V_M(r)$ being the atomic model potential [18] and with $|\psi_n^{(0)}\rangle$ being corresponding eigenkets. The summation in the Green function runs over the discrete and continuum states. The term of $G(\Omega)\hat{M}_{L,V}|\psi_g^{(0)}\rangle \equiv |\varphi_g\rangle$ is obtained by solving the Dalgarno–Lewis differential equation [19] as $(\Omega - \hat{H}_0)|\varphi_g\rangle = \hat{M}_{L,V}|\psi_g^{(0)}\rangle$, and $\Omega = \omega_g \mp \omega_{\text{IR}}$. To solve the equation, we apply the generalized pseudospectral method [20,21] with the detailed derivation in [22] and the modification for the boundary's error described in [23].

For the IR-dressed continuum state, both the CV and Volkov waves are considered:

$$\Psi_{\mathbf{k}}^{CV}(\mathbf{r}, t) = e^{-i\omega_{\mathbf{k}}t}e^{-i\boldsymbol{\alpha}_{\text{IR}}(t)\cdot\mathbf{k}}|\psi_{\mathbf{k}}^{(0)}\rangle, \quad (5a)$$

$$\Psi_{\mathbf{k}}^{V}(\mathbf{r}, t) = (2\pi)^{-3/2}k^{-1/2}e^{-i\omega_{\mathbf{k}}t}e^{-i\boldsymbol{\alpha}_{\text{IR}}(t)\cdot\mathbf{k}}e^{i\mathbf{k}\cdot\mathbf{r}}, \quad (5b)$$

where $\boldsymbol{\alpha}_{\text{IR}}(t) = c^{-1}\int_{-\infty}^{t}\mathbf{A}_{\text{IR}}(t')dt'$, $\mathbf{A}_{\text{IR}}(t)$ is the IR vector potential, $|\psi_{\mathbf{k}}^{(0)}\rangle = \sum_{l=0}^{\infty}\sum_{m=-l}^{l}i^l e^{-i(\sigma_l + \delta_l)}R_{El}(r)Y_{lm}(\Omega_{\mathbf{r}})Y_{lm}^*(\Omega_{\mathbf{k}})$, and $R_{El}(r) = \sqrt{\frac{2}{\pi k}}\frac{u_l(r)}{r}$. The factor $k^{-1/2}$ comes from the energy normalization. $E = k^2/2$ is the photoelectron energy, and σ_l and δ_l are the Coulomb and short-range phase shifts, respectively. The function $u_l(r)$ satisfies [24–26]

$$\left[-\frac{1}{2}\frac{d^2}{dr^2} + \frac{l(l+1)}{2r^2} + V_M(r) - \frac{k^2}{2}\right]u_l(r) = 0, \quad (6a)$$

$$u_l(r) \overset{r\to\infty}{\to} \sin\left[kr - \frac{l}{2}\pi - \frac{1}{k}\ln(2kr) + \sigma_l + \delta_l\right]. \quad (6b)$$

With the Jacobi–Anger expansion [27], the Volkov phase in Eq. (5a) or (5b) can be written as

$$e^{i\boldsymbol{\alpha}_{\text{IR}}(t)\cdot\mathbf{k}} = \sum_{n,m=-\infty}^{\infty} \tilde{J}_{n,m}e^{i(\pm n \pm m)(\omega_{\text{IR}}t + \phi_d)}, \quad (7)$$

where $\tilde{J}_{n,m} = i^{\pm m}J_n(\alpha_{\text{IR}}k|\cos\theta_{\mathbf{k}}|\cos\frac{\Delta}{2})J_m(\alpha_{\text{IR}}k|\sin\theta_{\mathbf{k}}| \cdot |\sin\phi_{\mathbf{k}}|\sin\frac{\Delta}{2})$, with α_{IR} being $E_{\text{IR}}/\omega_{\text{IR}}^2$ and J_n being the first-kind Bessel function. $+n$ holds for $\theta_{\mathbf{k}} \in [0, 0.5\pi]$, and

$-n$ for $\theta_{\mathbf{k}} \in [0.5\pi, \pi]$. $+m$ holds for $\phi_{\mathbf{k}} \in [0, \pi]$, and $-m$ for $\phi_{\mathbf{k}} \in [\pi, 2\pi]$.

By substituting the IR-dressed ground state in Eq. (4) and the continuum state in Eq. (5) into Eq. (1), with the help of Eq. (7), the zero-order $S_{L,V}$ matrix element due to the unperturbed ground state under the length (LG) and the velocity (VG) gauges can be expressed as, respectively,

$$S_L^{(0)}(\omega_{\mathbf{k}g}) = -i\langle \varphi_{\mathbf{k}}^{(0)} | \hat{z} \cdot \mathbf{r} | \psi_g^{(0)} \rangle \sum_{n,m=-\infty}^{\infty} \tilde{J}_{n,m} e^{i(\pm n \pm m)\phi_d}$$
$$\times F_{\mathrm{APT}}[-\omega_{\mathbf{k}g} - (\pm n \pm m)\omega_{\mathrm{IR}}], \qquad (8a)$$

$$S_V^{(0)}(\omega_{\mathbf{k}g}) = i\langle \varphi_{\mathbf{k}}^{(0)} | \hat{z} \cdot \nabla_{\mathbf{r}} | \psi_g^{(0)} \rangle \sum_{n,m=-\infty}^{\infty} \tilde{J}_{n,m} e^{i(\pm n \pm m)\phi_d}$$
$$\times \frac{F_{\mathrm{APT}}[-\omega_{\mathbf{k}g} - (\pm n \pm m)\omega_{\mathrm{IR}}]}{\omega_{\mathbf{k}g} + (\pm n \pm m)\omega_{\mathrm{IR}}}, \qquad (8b)$$

where $\varphi_{\mathbf{k}}^{(0)}$ is $|\psi_{\mathbf{k}}^{(0)}\rangle$ or $(2\pi)^{-3/2}k^{-1/2}e^{i\mathbf{k}\cdot\mathbf{r}}$ for the CV wave and Volkov wave, respectively. $F_{\mathrm{APT}}(\omega)$ denotes the Fourier transform of the APT electric field in Eq. (2) and $\omega_{\mathbf{k}g} = \omega_{\mathbf{k}} - \omega_g$. The rule for the sign of index n and m is the same as that in Eq. (7). The angular quantum number of the continuum state $l = 1$ for He, while $l = 0, 2$ for Ar.

The first-order S matrix element due to the perturbed ground state can be expressed as

$$S_L^{(1)}(\omega_{\mathbf{k}g}) = \frac{E_{\mathrm{IR}}}{2} \sum_{n,m=-\infty}^{\infty} \tilde{J}_{n,m}$$
$$\times \Bigg\{ -e^{i(\pm n \pm m + 1)\phi_d} F_{\mathrm{APT}}[-\omega_{\mathbf{k}g} - (\pm n \pm m + 1)\omega_{\mathrm{IR}}]$$
$$\times \langle \varphi_{\mathbf{k}}^{(0)} | \hat{z} \cdot \mathbf{r} | G(\omega_g - \omega_{\mathrm{IR}}) \hat{z} \cdot \mathbf{r} \psi_g^{(0)} \rangle$$
$$+ e^{i(\pm n \pm m - 1)\phi_d} F_{\mathrm{APT}}[-\omega_{\mathbf{k}g} - (\pm n \pm m - 1)\omega_{\mathrm{IR}}]$$
$$\times \langle \varphi_{\mathbf{k}}^{(0)} | \hat{z} \cdot \mathbf{r} | G(\omega_g + \omega_{\mathrm{IR}}) \hat{z} \cdot \mathbf{r} \psi_g^{(0)} \rangle \Bigg\}, \qquad (9a)$$

$$S_V^{(1)}(\omega_{\mathbf{k}g}) = \frac{E_{\mathrm{IR}}}{2\omega_{\mathrm{IR}}} \sum_{n,m=-\infty}^{\infty} \tilde{J}_{n,m}$$
$$\times \Bigg\{ e^{i(\pm n \pm m + 1)\phi_d} \frac{F_{\mathrm{APT}}[-\omega_{\mathbf{k}g} - (\pm n \pm m + 1)\omega_{\mathrm{IR}}]}{\omega_{\mathbf{k}g} + (\pm n \pm m + 1)\omega_{\mathrm{IR}}}$$
$$\times \langle \varphi_{\mathbf{k}}^{(0)} | \hat{z} \cdot \nabla_{\mathbf{r}} | G(\omega_g - \omega_{\mathrm{IR}}) \hat{z} \cdot \nabla_{\mathbf{r}} \psi_g^{(0)} \rangle$$
$$+ e^{i(\pm n \pm m - 1)\phi_d} \frac{F_{\mathrm{APT}}[-\omega_{\mathbf{k}g} - (\pm n \pm m - 1)\omega_{\mathrm{IR}}]}{\omega_{\mathbf{k}g} + (\pm n \pm m - 1)\omega_{\mathrm{IR}}}$$
$$\times \langle \varphi_{\mathbf{k}}^{(0)} | \hat{z} \cdot \nabla_{\mathbf{r}} | G(\omega_g + \omega_{\mathrm{IR}}) \hat{z} \cdot \nabla_{\mathbf{r}} \psi_g^{(0)} \rangle \Bigg\}, \qquad (9b)$$

where the angular quantum number of the continuum state differs from that of Eqs. (8a) and (8b) due to the perturbed ground state. Here $l = 0, 2$ for He, while $l = 1, 3$ for Ar.

Finally, the transition probability can be calculated by $|S_{L,V}^{(0)}(\omega_{\mathbf{k}g}) + S_{L,V}^{(1)}(\omega_{\mathbf{k}g})|^2$.

3. RESULTS AND DISCUSSION

We consider the APT and IR intensities of 5×10^{13} W/cm^2 and 10^{13} W/cm^2, respectively. The APT is characterized by

$\tau_x = 0.3$ fs, $\tau_T = 3$ fs, and $\omega_x = 35$ eV for He, and $\omega_x = 26$ eV for Ar. With such ω_x choice, the central photoelectron energy ionized by the APT for He ($E_i \approx 24.6$ eV) and for Ar ($E_i \approx 15.76$ eV) is about 10 eV, where E_i is the ionization potential. The atomic potential is adapted from Tong and Lin [18]. The ground-state wave function of He (1s) is assumed as $2\alpha^{1.5} \exp(-\alpha r)$ with $\alpha = 1.67$, while that of Ar (3p) is obtained numerically.

First, we consider the contribution from the unperturbed term $S_{L,V}^{(0)}(\omega)$. Figure 2(a) shows the photoelectron spectra of He under the LG (dotted curve) and VG (solid curve) for the IR delay phase $\phi_d = 0.5\pi$. The CV results (left panel) give good agreement between the LG and the VG, while the Volkov results (right panel) show an evident gauge difference. Each spectral peak separated by ω_{IR} instead of $2\omega_{\mathrm{IR}}$ as shown in Fig. 1(b) manifests that a single XUV photon with multiple-IR-photon processes occurs. The photoelectrons are localized around the central APT's excitation about 10 eV, and thus we call it *one-group behavior*. Figure 2(b) shows the spectrum in He at the IR delay phase $\phi_d = 0$. Here, both the CV and Volkov results have gauge differences, but the CV results show a better agreement than the Volkov results. At $\phi_d = 0$, the photoelectrons drift away from the central APT's excitation and then result in *two-group behavior*, where one is a low-energy group (<10 eV) and the other is a high-energy group (>10 eV). Because of the high-energy group, the photoelectron spectra at $\phi_d = 0$ has a more extended distribution than that at $\phi_d = 0.5\pi$.

Figures 2(c) and (d) show the photoelectron spectra of Ar for $\phi_d = 0.5\pi$ and 0, respectively. At $\phi_d = 0.5\pi$, the CV results remain in good gauge agreement, while for the Volkov results, the gauge difference enlarges clearly as compared with the He case. At $\phi_d = 0$, the CV results still keeps a low gauge difference, while for the Volkov results, the gauge difference becomes significantly large. Thus, the CV wave is better than the Volkov wave in modeling the IR-dressed continuum states of both atoms. Otherwise, there is an essential spectral difference between the two atoms at $\phi_d = 0$. The amplitude ratio of the high-energy to low-energy groups in Ar is clearly lower than that in He. This can be easily understood by the analytic theory because the dipole matrix element in Eq. (8a) of Ar (solid curve) decreases with photoelectron energy faster than that of He (dashed curve) as shown in the inset of Fig. 2(d).

Next, we consider the contribution from the perturbed term $S_{L,V}^{(1)}(\omega)$. Under the LG, the perturbed term is always negligible due to the small E_{IR} (0.017 a.u.) and the tiny difference between the functions of $G(\omega_g \mp \omega_{\mathrm{IR}})\hat{\epsilon} \cdot \mathbf{r}\psi_g^{(0)}$ in Eq. (9a). Under the VG, the perturbed term is visible when $\phi_d = 0$. Figure 3(a) shows the spectral results with (solid curve) and without (dotted curve) the perturbed term in He. The result with the perturbed term below (above) 10 eV is lower (higher) than the result without the perturbed term. As compared with Fig. 2(b), the perturbed term amplifies the CV gauge difference, except the peak near 10 eV. This manifests that the CV gauge difference in Fig. 2(b) is not due to the perturbed ground state, but it is due to the inaccuracy of the CV wave. If the CV wave is substituted by an exact dressed continuum state, the CV gauge difference can be eliminated and the corresponding VG perturbation should also become evanescent. While the gauge difference at $\phi_d = 0$ is not large [28], the CV
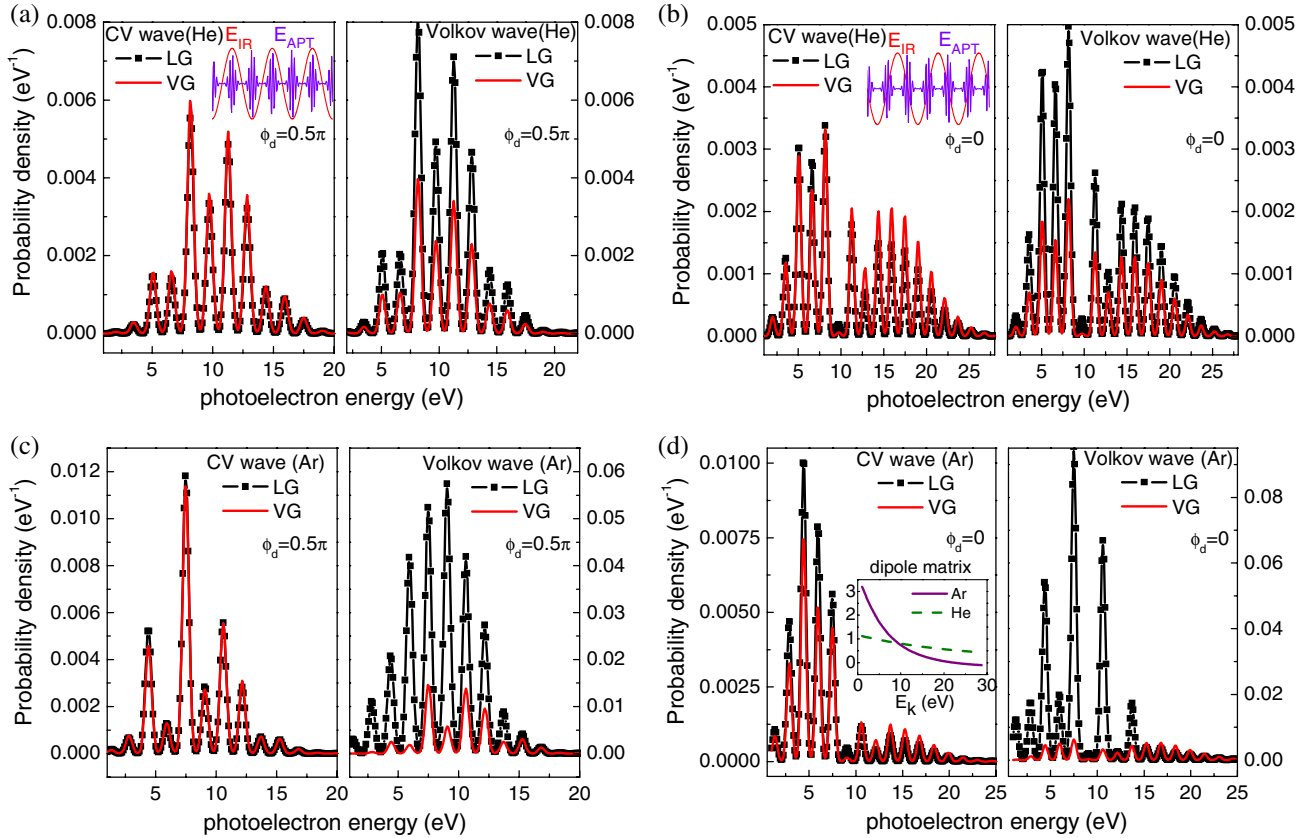
Fig. 2. (Color online) CV and Volkov photoelectron spectra under the LG (dotted curves) and VG (solid curves) for (a) He at $\phi_d = 0.5\pi$, (b) He at $\phi_d = 0$, (c) Ar at $\phi_d = 0.5\pi$, and (d) Ar at $\phi_d = 0$. $I_{\text{APT}} = 5 \times 10^{13}$ W/cm^2, $\tau_x = 0.3$ fs, $\tau_T = 3$ fs, and $\omega_x = 35$ eV for He, and $\omega_x = 26$ eV for Ar. $I_{\text{IR}} = 10^{13}$ W/cm^2 and $\omega_{\text{IR}} = 1.55$ eV. Insets of (a) and (b) show schematic diagrams for delay phases between IR and APT electric fields. Inset of (d) shows the dipole matrix element $\langle \varphi_{\mathbf{k}}^{(0)} | \hat{z} \cdot \mathbf{r} | \psi_g^{(0)} \rangle$ in Eq. (8a) for He ($l = 1$: dashed curve) and Ar ($l = 2$: solid curve; $l = 0$: minor not shown). The photoelectron spectra are integrated over solid angle.

wave is still a good approximation as long as the IR intensity keeps at an appropriate level.

Figure 3(b) shows the result with the perturbed term in Ar. For the CV result, the perturbation dependence on the photoelectron energy is consistent with that of He, but not for the Volkov result. This also manifests that the CV wave is more reliable than the Volkov wave. Finally, we exam the CV result with the TDSE calculation shown in Fig. 3(c). The TDSE result also shows the one-group and two-group behaviors at $\phi_d = 0.5\pi$ and 0, respectively. The CV result agrees with the TDSE one qualitatively, except the fact that, at $\phi_d = 0$, the valley between the low-energy and high-energy groups in the TDSE result is not as deep as that in the CV. Quantitatively, a slight difference between the CV and TDSE results can be obtained.

After examining the CV wave and the ground-state perturbation, we now apply the theory to study the IR polarization effect, which can be understood by using the concept of one-group and two-group behaviors. While the concept is the consequence of electron-wave-packet interference, we first show the angular distribution of interferometry with various IR polarizations [6,7]. For comparison, the case of $\mathbf{E}_{\text{IR}} \| \mathbf{E}_{\text{XUV}}$ is shown. The calculation is performed in He under the LG. Figure 4(a) shows the angular distribution of a photoelectron by an XUV burst without the IR field. If the burst is at the zero of $\mathbf{A}_{\text{IR}}(t)$ ($\phi_d = 0.5\pi$), the burst-excited electron gains no momentum from the IR field [Fig. 4(b)], as the semiclassical

theory predicts photoelectrons momentum transferred by $|A_{\text{IR}}(t)|/c$. The distribution stays ring-shaped and centered at the origin, similar to Fig. 4(a). Thus, the interference of electron wave packets excited by double bursts makes the distribution one-group behavior [Fig. 4(c)]. Otherwise, if the burst is at the peak of $\mathbf{A}_{\text{IR}}(t)$ ($\phi_d = 0$), the burst-excited electron shifts along the k_z axis due to the IR field [Fig. 4(d)], and thus leads the distribution to split into two groups (one toward higher k_z and the other lower) as double bursts are excited [Fig. 4(e)].

For the perpendicular case ($\mathbf{E}_{\text{IR}} \| \hat{y}$ and $\mathbf{E}_{\text{XUV}} \| \hat{z}$), the XUV burst becomes born at the peak of $\mathbf{A}_{\text{IR}}(t)$ for $\phi_d = 0.5\pi$ and born at the zero of $\mathbf{A}_{\text{IR}}(t)$ for $\phi_d = 0$ according to Eq. (3). Interestingly, the electron excited by the burst at the peak of $\mathbf{A}_{\text{IR}}(t)$ does not shift along the k_y axis, as the semiclassical theory predicts, but it shrinks [Fig. 4(f)] or elongates [Fig. 4(g)] at the maximum or minimum of $\mathbf{A}_{\text{IR}}(t)$, respectively. Hence, the interference of electron wave packets excited by the double XUV bursts also leads the distribution to split into two groups [Fig. 4(h)] along the k_y axis. Otherwise, if the burst is at the zero of $\mathbf{A}_{\text{IR}}(t)$, the angular distribution [Fig. 4(i)] does not change much, and the distribution remains in one group as the double bursts are excited [Fig. 4(j)]. For the circular IR polarization, the result is like the combination of the parallel and perpendicular cases. At $\phi_d = 0.5\pi$, the angular distribution is dominated by A_y (dashed curve). Thus, the distribution shrinks [Fig. 4(k)] or elongates [Fig. 4(l)] for the XUV burst at
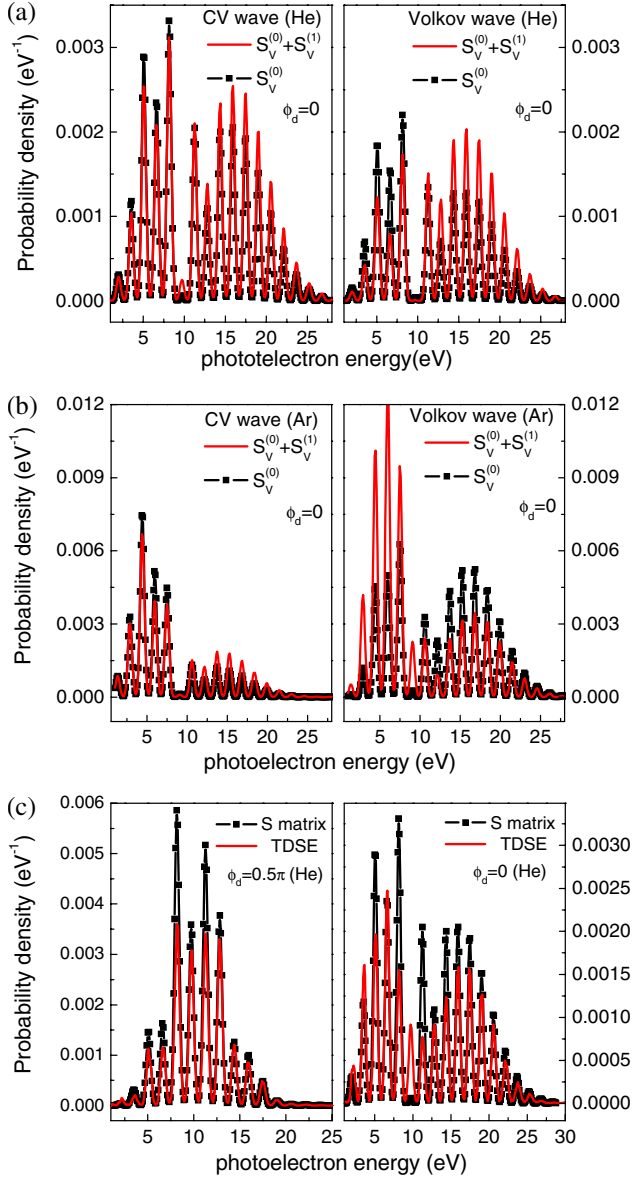
Fig. 3. (Color online) Unperturbed (dotted curve) and perturbed (solid curve) photoelectron spectra integrated over solid angle under the VG for (a) He at $\phi_d = 0$ and (b) Ar at $\phi_d = 0$. Other optical conditions are the same as those in Fig. 2. (c) Comparison of spectra in He between the TDSE calculations (solid curve) and *S*-matrix results (dotted curve) of CV waves.

the peak of A_y, and the two-group behavior along the k_y axis results as double bursts are excited [Fig. 4(m)], just as in the perpendicularly polarized case. At $\phi_d = 0$, the angular distribution becomes dominated by A_z (solid curve) [Fig. 4(n)]. The distribution shifts toward the k_z axis for the burst at the peak of A_z, and finally two groups along the k_z axis result as double bursts are excited [Fig. 4(o)], which resembles the parallel polarized case.

With the above understanding of interference, we now can see the IR polarization effect on the photoelectron spectrum. Figure 5(a) shows the APT-excited spectrum as a function of IR delay phase in He for the case of $E_{IR} \| E_{XUV}$ under the LG. Two-group behavior around $\phi_d = \kappa\pi$ (κ is an integer) is shown clearly. As ϕ_d moves to $(\kappa + 0.5)\pi$, the spectrum becomes one-group behavior. For the case of $E_{IR} \perp E_{XUV}$, the two-group

behavior shifts to the delay phase of $(\kappa + 0.5)\pi$, as shown in Fig. 5(b) as predicted earlier in Figs. 4(f)–(j). The spectral extension to higher (or lower) energies than the central APT's excitation in Fig. 5(b) is weaker than that in Fig. 5(a). In the $E_{IR} \| E_{APT}$ case, the spectrum at $\phi_d = 0$ can extend to higher energies with a five-IR-photon difference than that at $\phi_d = 0.5\pi$, while, in the $E_{IR} \perp E_{APT}$ case, there is a three-IR-photon difference. Therefore, the IR parallel polarization has an only slightly higher capability of quantum control than the perpendicular case.

Figure 5(c) shows the APT-excited spectrum with the circular IR polarization. The pattern is like the superposition of the $E_{IR} \| E_{APT}$ and $E_{IR} \perp E_{APT}$ cases, as Figs. 4(k)–(o) describe. Around $\phi_d = (\kappa + 0.5)\pi$, the parallel and perpendicular IR fields contribute to the one-group and the two-group spectra, respectively. As ϕ_d becomes around $\kappa\pi$, the parallel and perpendicular IR fields turn to contribute to the two-group and one-group spectra, respectively. As a result, the spectrum becomes broad and full at any IR delay phase, implying a much lower capability of quantum control than that of linear IR polarizations. Regarding the species issue, He has a higher controlling capability than Ar, as shown in Fig. 5(d). In Ar, there is an only three-IR-photon spectral difference between $\phi_d = 0$ and 0.5π for the $E_{IR} \| E_{APT}$ case. This is attributed to the faster decay of the dipole matrix in Ar than He, as shown in the inset of Fig. 2(d).

To compare with the experimental result, we also show the Ar spectrum in Fig. 5(e) with the same conditions as those in [5], where $I_{IR} = 3 \times 10^{13}$ W/cm^2 and $\tau_x = 0.2$ fs to include the IR harmonics 13 through 35, and ω_x is at the middle of these harmonics. First, the spectral dependence agrees with the experimental results qualitatively. The photoelectrons at $\phi_d = (\kappa + 0.5)\pi$ are confined around the central APT's excitation, while the photoelectrons at $\phi_d = \kappa\pi$ have a more extended energy distribution. Second, at $\phi_d = (\kappa + 0.5)\pi$, our maximum photoelectron energy is about 28 eV and is close to the experimental result. At $\phi_d = (\kappa + 0.5)\pi$, the maximum energy extends over 40 eV. This resembles their TDSE result, but it is higher than the experimental one [5]. Third, in our calculation, the central photoelectron energy ionized by the APT is 20 eV. This value is about 5 eV higher than the experimental one. This is probably due to our APT modeling with a Gaussian shape in the energy domain [Fig. 1(b)], while the actual APT is synthesized from harmonics in plateau with equal height. The effect also causes our spectrum to decay quickly as the photoelectron energy approaches zero.

Although the circular IR polarization is too weak to control the spectrum, its photoelectron's angular distribution is much richer than that of linear IR polarizations. Figures 6(a)–(c) show the angular distributions of photoelectrons in He under the LG of circular polarization at various IR delay phases, where the arrow denotes the z-axis direction. At the zero delay phase [Fig. 6(a)], both upper (azimuthal angle $\theta_k \leq 0.5\pi$) and lower ($\theta_k > 0.5\pi$) spheres have the same dependence on the polar angle ϕ_k. For brevity, we call it ϕ_k symmetry for $P(\theta_k, \phi_k) = P(\pi - \theta_k, \phi_k)$, where P is the probability density. The photoelectron is strong around $\phi_k = (\kappa + 0.5)\pi$, and evanescent around $\phi_k = \kappa\pi$. Thus, there are two nodes along the ϕ_k direction. The symmetry changes when the delay phase varies. At the delay phase of 0.25π [Fig. 6(b)], the symmetry becomes antisymmetry $P(\theta_k, -\phi_k) = P(\pi - \theta_k, \phi_k)$. The
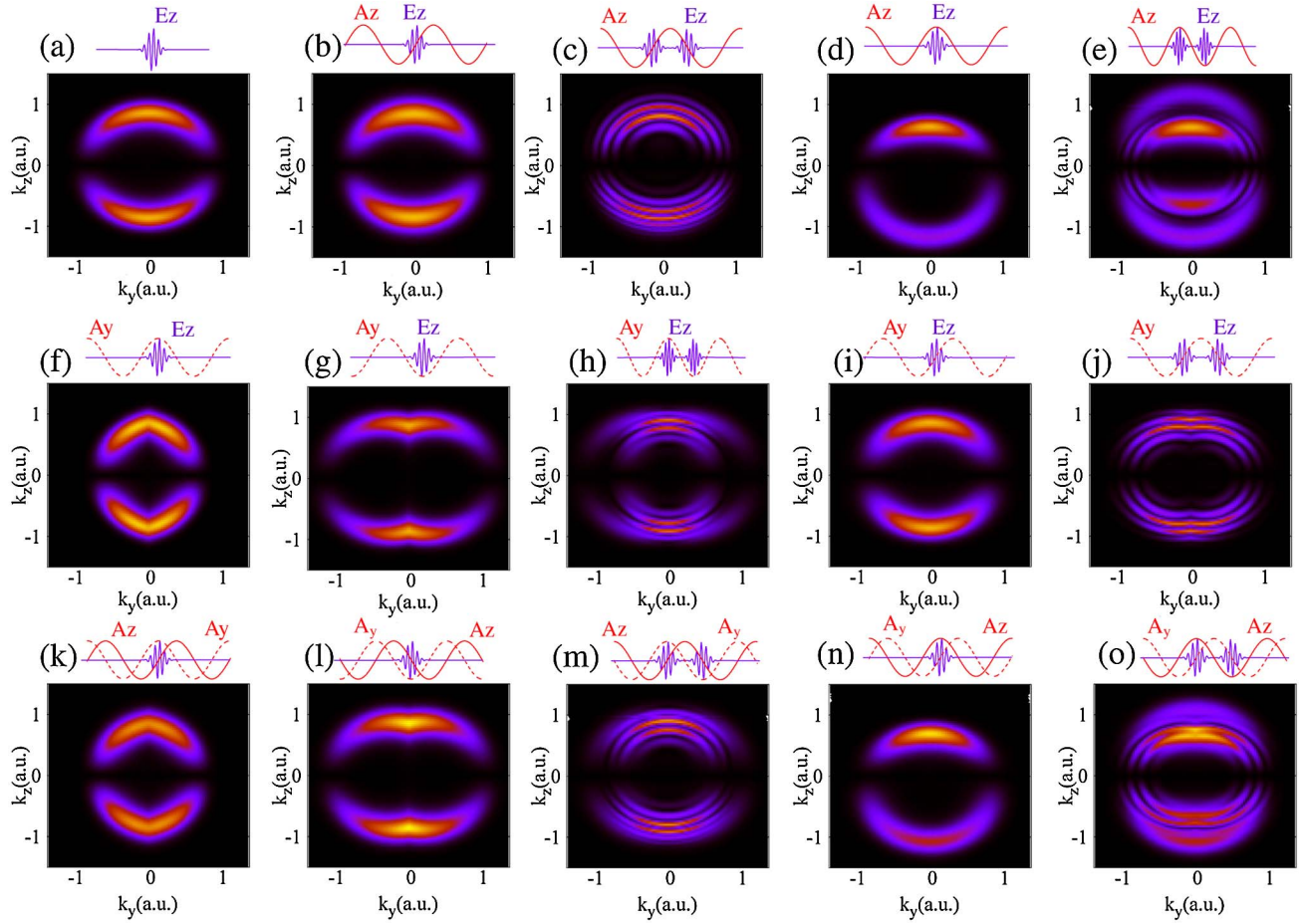
Fig. 4. (Color online) Angular distribution of photoelectrons for (a)–(e) $\mathbf{E}_{IR} \| \mathbf{E}_{XUV}$, (f)–(j) $\mathbf{E}_{IR} \perp \mathbf{E}_{XUV}$, and (k)–(o) circular IR polarization in He under the LG. E_z: APT's electric field (solid curve in purple). A_z: z-component IR magnetic vector potential (solid curve in red). A_y: y-component IR vector potential (dashed curve in red).

upper sphere has an opposite $\phi_\mathbf{k}$ dependence to the lower sphere. In addition, the photoelectron does not vanish along the $\phi_\mathbf{k}$ direction, i.e., there is no node, unlike that at the zero delay phase. At the delay phase of 0.5π [Fig. 6(c)], the $\phi_\mathbf{k}$ symmetry is retrieved, but the photoelectron always stays brilliant along the polar direction. The strongest and the weakest photoelectrons are around $\phi_\mathbf{k} = \kappa\pi$ and $(\kappa + 0.5)\pi$, respectively. As we can see, the three distinct delay phases result in three quite different angular distributions. In contrast, the angular distribution of linear IR polarization is simple. Figures 6(d) and (e) show the results in He under the LG of $\mathbf{E}_{IR} \perp \mathbf{E}_{APT}$ at the delay phases of 0, 0.25π, and 0.5π, respectively. The three results are similar. All of them are $\phi_\mathbf{k}$ symmetry and have two nodes at $\phi_\mathbf{k} = \kappa\pi$. For the $\mathbf{E}_{IR} \| \mathbf{E}_{APT}$ case, the angular distribution is the simplest among the three cases since its S matrix is independent of $\phi_\mathbf{k}$ ($\Delta = 0$), which is related only to $\theta_\mathbf{k}$. Hence, the priority about the angular distribution becomes the circular, perpendicular, and parallel polarizations.

4. CONCLUSION

In conclusion, we theoretically studied the IR-dressed XUV transition in He and Ar atoms by applying the perturbation theory to the ground state and considering the CV wave. The CV wave can much reduce the gauge inconsistency calculated with the Volkov wave. The contribution of ground-state perturbation to the photoelectron spectra is generally negligible, and the spectra are more sensitive to the dressed continuum states than the perturbed ground state. Our results agree with the experimental results of Johnsson *et al.* [5] qualitatively. The considerable spectral dependence on the delay phase between the IR and the APT fields is shown. As the APT's burst is at the zero of A_{IR}, the photoelectrons are localized around the central APT's excitation, and result in the one-group behavior. As the burst is at the peak of A_{IR}, the photoelectrons drift away from the central APT's excitation, and result in the two-group behavior. The amplitude ratio of high- to low-energy groups is lower in Ar than in He. The photoelectron spectrum is also sensitive to the IR polarization. Linear IR polarizations ($\mathbf{E}_{IR} \| \mathbf{E}_{APT}$ and $\mathbf{E}_{IR} \perp \mathbf{E}_{APT}$) have a stronger spectral dependence on the IR delay phase than the circular IR polarization. Among the three polarizations, the $\mathbf{E}_{IR} \| \mathbf{E}_{APT}$ case is the best at controlling the XUV-induced photoelectron spectrum. On the other hand, the circular IR polarization can result in a more fruitful angular dependence of photoelectrons than linear polarizations, while the $\mathbf{E}_{IR} \| \mathbf{E}_{APT}$ case has the simplest angular distribution among them.

ACKNOWLEDGMENTS
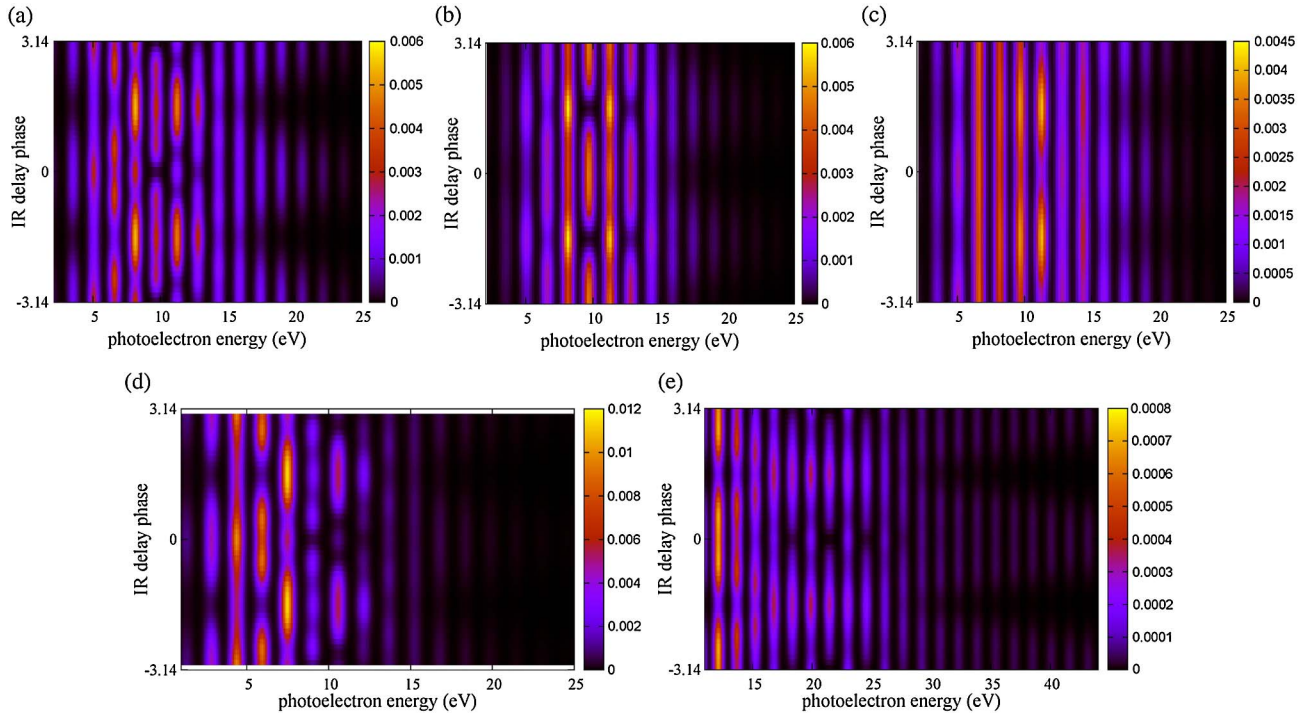
Fig. 5.   (Color online) Photoelectron spectra as a function of IR delay phase under the LG for (a) $\mathbf{E}_{IR} \| \mathbf{E}_{APT}$ in He, (b) $\mathbf{E}_{IR} \perp \mathbf{E}_{APT}$ in He, (c) circular IR polarization in He, and (d) $\mathbf{E}_{IR} \| \mathbf{E}_{APT}$ in Ar. Other optical conditions are the same as those in Fig. 2. (e) Simulation of Ar for comparison with the experimental result of Johnsson *et al.* [5], where $\mathbf{E}_{IR} \| \mathbf{E}_{APT}$, $I_{IR} = 3 \times 10^{13}$ W/cm^2, and $\tau_x = 0.2$ fs to include the IR harmonics 13 through 35, and the APT's central frequency at harmonic 24 ($\omega_x = 37.2$ eV). All spectra are integrated over solid angle.
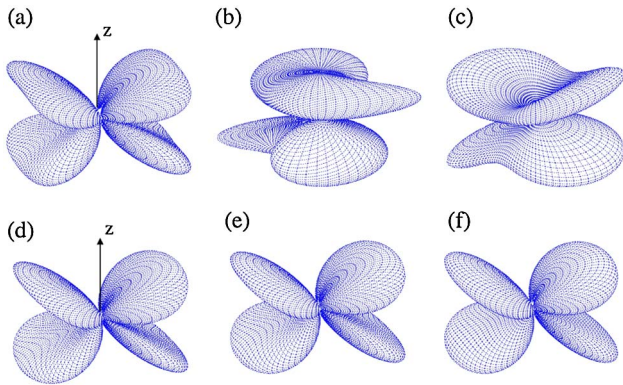

Fig. 6.   (Color online) Angular distribution of photoelectron in He under the LG for the IR circular polarization at (a) $\phi_d = 0$, (b) $\phi_d = 0.25\pi$, and (c) $\phi_d = 0.5\pi$; and for $\mathbf{E}_{IR} \perp \mathbf{E}_{APT}$ at (d) $\phi_d = 0$, (e) $\phi_d = 0.25\pi$, and (f) $\phi_d = 0.5\pi$. The arrow denotes the z-axis direction. Other optical conditions are the same as those in Fig. 2.

REFERENCES

1. F. Krausz and M. Ivanov, "Attosecond physics," Rev. Mod. Phys. **81**, 163–234 (2009).
2. P. B. Corkum and F. Krausz, "Attosecond science," Nat. Phys. **3**, 381–387 (2007).
3. H. G. Muller, "Reconstruction of attosecond harmonic beating by interference of two-photon transitions," Appl. Phys. B **74**, S17–S21 (2002).
4. Y. Mairesse, A. Bohan, L. J. Frasinski, H. Merdji, L. C. Dinu, P. Monchicourt, P. Breger, M. Kovačev, R. Taieb, B. Carré, H. G. Muller, P. Agostini, and P. Salières, "Attosecond synchronization of high-harmonic soft X-rays," Science **302**, 1540–1543 (2003).
5. P. Johnsson, R. López-Martens, S. Kazamias, J. Mauritsson, C. Valentin, T. Remetter, K. Varjú, M. B. Gaarde, Y. Mairesse, H. Wabnitz, P. Salières, P. Balcou, K. J. Schafer, and A. L'Huillier, "Attosecond electron wave packet dynamics in strong laser fields," Phys. Rev. Lett. **95**, 013001 (2005).
6. T. Remetter, P. Johnsson, J. Mauritsson, K. Varjú, Y. Ni, F. Lépine, E. Gustafsson, M. Kling, J. Khan, R. López-Martens, K. J. Schafer, M. J. J. Vrakking, and A. L'Huillier, "Attosecond electron wave packet interferometry," Nat. Phys. **2**, 323–326 (2006).
7. K. Varjú, P. Johnsson, J. Mauritsson, T. Remetter, T. Ruchon, Y. Ni, F. Lépine, M. Kling, J. Khan, K. J. Schafer, M. J. J. Vrakking, and A. L'Huillier, "Angularly resolved electron wave packet interferences," J. Phys. B **39**, 3983–3991 (2006).
8. P. Johnsson, J. Mauritsson, T. Remetter, A. L'Huillier, and K. J. Schafer, "Attosecond control of ionization by wave-packet interference," Phys. Rev. Lett. **99**, 233001 (2007).
9. L. Y. Peng, E. A. Pronin, and A. F. Starace, "Attosecond pulse carrier-envelope phase effects on ionized electron momentum and energy distributions: roles of frequency, intensity and additional IR pulse," New J. Phys. **10**, 025030 (2008).
10. X. M. Tong, P. Ranitovic, C. L. Cocke, and N. Toshima, "Mechanisms of infrared-laser-assisted atomic ionization by attosecond pulses," Phys. Rev. A **81**, 021404(R) (2010).
11. J. Mauritsson, T. Remetter, M. Swoboda, K. Klünder, A. L'Huillier, K. J. Schafer, O. Ghafur, F. Kelkensberg, W. Siu, P. Johnsson, M. J. J. Vrakking, I. Znakovskaya, T. Uphues, S. Zherebtsov, M. F. Kling, F. Lépine, E. Benedetti, F. Ferrari, G. Sansone, and M. Nisoli, "Attosecond electron spectroscopy using a novel interferometric pump-probe technique," Phys. Rev. Lett. **105**, 053001 (2010).
12. F. Kelkensberg, W. Siu, J. F. Pérez-Torres, F. Morales, G. Gademann, A. Rouzée, P. Johnsson, M. Lucchini, F. Calegari, J. L. Sanz-Vicario, F. Martín, and M. J. J. Vrakking, "Attosecond control in photoionization of hydrogen molecules," Phys. Rev. Lett. **107**, 043002 (2011).

13. A. Maquet and R. Taïeb, "Two-colour IR + XUV spectroscopies: the 'soft-photon approximation'," J. Mod. Opt. **54**, 1847–1857 (2007).

14. F. Ehlotzky, "Atomic phenomena in bichromatic laser fields," Phys. Rep. **345**, 175–264 (2001).

15. D. B. Milošević and F. Ehlotzky, "X-ray photoionization in the presence of bichromatic laser field," Phys. Rev. A **57**, 2859–2866 (1998).

16. A. Cionga, V. Florescu, A. Maquet, and R. Taïeb, "Target dressing effects in laser-assisted x-ray photoionization," Phys. Rev. A **47**, 1830–1840 (1993).

17. C. J. Joachain, P. Francken, A. Maquet, P. Martin, and V. Veniard, "(*e*, 2*e*) collisions in the presence of a laser field," Phys. Rev. Lett. **61**, 165–168 (1988).

18. X. M. Tong and C. D. Lin, "Empirical formula for static field ionization rates of atoms and molecules by lasers in the barrier-suppression regime," J. Phys. B **38**, 2593–2600 (2005).

19. A. Dalgarno and J. T. Lewis, "Exact calculation of long-range forces between atoms by perturbation theory," Proc. R. Soc. London Ser. A **233**, 70–74 (1955).

20. J. Shen and T. Tang, *Spectral and High-Order Methods with Applications* (Science, 2006).

21. C. Canuto, M. Y. Hussaini, A. Quarteroni, and T. A. Zang, *Spectral Methods in Fluid Dynamics* (Springer-Verlag, 1988).

22. D. A. Telnov and S. I. Chu, "Multiphoton detachment of H⁻ near the one-photon threshold: exterior complex scaling generalized pseudospectral method for complex quasienergy resonances," Phys. Rev. A **59**, 2864–2874 (1999).

23. A. Bayliss, A. Class, and B. J. Matkowsky, J. Comput. Phys. **116**, 380–383 (1995).

24. H. Friedrich, *Theoretical Atomic Physics* (Springer, 1998), p. 29 and p. 219.

25. C. J. Joachain, "The Coulomb potential," in *Quantum Collision Theory* (North-Holland, 1975), pp. 134–160.

26. L. I. Schiff, "Continuous eigenvalues: collision theory," in *Quantum Mechanics* (McGraw-Hill, 1968), pp. 100–147.

27. G. A. Korn and T. M. Korn, *Mathematical Handbook for Scientists and Engineers* (McGraw-Hill, 1961), p. 732.

28. J. Zhang and T. Nakajima, "Coulomb effects in photoionization of H atoms irradiated by intense laser fields," Phys. Rev. A **75**, 043403 (2007).